Atomistic mechanism for vacancy-enhanced grain boundary migration

Dengke Chen

Woodruff School of Mechanical Engineering, Georgia Institute of Technology, Atlanta, Georgia 30332, USA

Shuozhi Xu

California NanoSystems Institute, University of California, Santa Barbara, California 93106, USA

Yashashree Kulkarni[*]

Department of Mechanical Engineering, University of Houston, Houston, Texas 77004, USA

Mechanical behavior of polycrystalline materials is intimately connected to migration of grain boundaries, which in turn is dramatically impacted by the presence of defects. In this paper, we present atomistic simulations to elucidate the elementary mechanism that dictates the role of vacancies in enhancing grain boundary migration via shear-coupled normal motion. The minimum energy pathway and the associated energy barriers are calculated using the nudged elastic band method. Fully three-dimensional atomistic simulations provide excellent verification of the three-dimensional disconnection model and furnish quantitative evidence that vacancies facilitate grain boundary migration by weakening the line tension of a disconnection loop. It is also revealed that vacancies serve as energetically favorable sites for the nucleation of grain boundary disconnections, thereby inducing shear-coupled grain boundary migration.

I. INTRODUCTION

Grain boundaries (GBs) are key players in the plasticity, damage, and failure of polycrystalline materials [1–3]. A quantitative description of GB-mediated processes, such as migration, sliding, and defect interactions, is hence vital for optimizing the properties of the polycrystal through mechanical processing and has been the subject of long-standing interest [4–19].

At low temperatures, a dominant mechanism for GB migration for a certain class of GBs, specifically, the coincident site lattice (CSL) GBs, is known to be the shear-coupled normal motion [20,21]. Shear-coupled normal motion occurs by the displacement of the GB normal to its plane due to resolved shear stress parallel to the GB plane. The motion is quantified by a geometric factor known as the coupling factor, $\beta = v_{||}/v_n$, which refers to the ratio between the applied shear velocity $v_{||}$ and the resulting normal GB velocity v_n. Several studies in recent years have provided insights into the dependence of the shear-coupled migration on GB geometry, temperature, and applied shear stress [20–28].

Using the nudged elastic band (NEB) method [29,30], Combe and coworkers [24] investigated the migration of a $\Sigma 13(320)$ GB in a copper bicrystal. They provided detailed evidence that thermally activated two-dimensional (2D) shear-coupled GB migration occurs through a pair of parallel disconnections, each consisting of a dislocation and a step [4,31].

However, three-dimensional (3D) disconnection theory [4], which, in principle, is closer to reality, is still confined to theoretical analysis and has not been verified through atomistic simulations or experiments to the best of our knowledge.

In addition, studies have probed the influence of impurities on GB motion [32–35] since GBs are known to be effective sinks for defects, especially point defects. Conventional understanding is that point defects, including vacancies, interstitials, and substitutional atoms, have a drag effect, thereby hindering GB migration [32]. Quite interestingly, some recent studies have reported that vacancies might enhance GB sliding [33] or bcc twin migration [36]. Thus, there is a need to investigate the elementary mechanism that leads to this rather unusual phenomenon by which vacancies might promote GB motion.

In the present study, we employ NEB simulations to provide verification of the 3D disconnection theory for GB migration. Furthermore, our NEB calculations elucidate the role of vacancies in shear-coupled migration of a certain class of GBs. It is revealed that vacancies facilitate the nucleation of GB disconnections by weakening the line tension of the disconnection loop and lowering the energy barrier for shear-coupled migration. The detailed elementary mechanism for the process is furnished by quasi-2D NEB calculations. The rest of the paper is organized as follows. In Sec. II, we describe the 3D simulation setup, details of the NEB calculations, and formation energies for various vacancy sites in the GB. In Sec. III, we provide the representative 3D NEB results for GB migration with and without vacancies and investigate the effect of vacancy distribution and numbers. Section IV
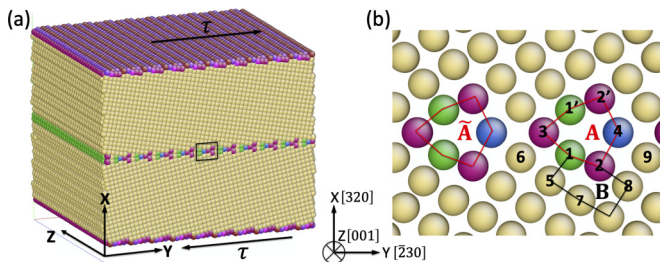
---

*ykulkarni@uh.edu

FIG. 1. (a) Atomistic structure of the simulation cell showing a GB in an fcc bicrystal. (b) Atomistic configuration of the $\Sigma 13(320)$ GB projected in the (X, Y) plane. Atoms are colored according to the coordination number (CN; green: CN = 10; red: CN = 11; yellow: CN = 12; blue: CN = 13). Candidate vacancy sites around a repeating kite-shaped structural unit are labeled from 1 to 9; 1' and 2' are sites symmetric to 1 and 2, respectively.

reveals the mechanism of vacancy-enhanced migration through atomistic and mesoscopic views and verifies the phenomenon through molecular dynamics (MD) simulations at room temperature. The summary and potential ramifications of these findings are discussed in Sec. V.

II. SIMULATION METHODS

A. Simulation setup

For our 3D atomistic simulations, we consider a copper bicrystal with a $\Sigma 13(320)$ symmetric tilt GB subjected to shear deformation [Fig. 1(a)]. Our choice of this particular GB is dictated by the fact that it is a CSL boundary exhibiting shear-coupled normal motion, and its migration has been studied in 2D simulations previously [24]. All simulations are performed using the simulation package LAMMPS [37]. The embedded atom method (EAM) interatomic potential by Mishin *et al.* [38] is employed. Periodic boundary conditions are imposed in the lateral (Y and Z) directions, whereas a fixed boundary condition is imposed in the X direction. Two 1.5-nm-thick slabs are fixed at the top and the bottom of the simulation cell and serve to exert the applied shear stress τ. Only the dynamic atoms within the simulation cell participate in the molecular statics simulations. The size of the 3D simulation cell is $103 \times 130 \times 123 \, \text{Å}^3$.

B. NEB simulation details

N (48) replicas were used to describe the minimum energy path (MEP). By initial configurations we mean the initial N replicas. After several time steps, they would converge to final configurations and replicas. For each time step, there are N replicas, including first replica and end replica. The first and end replicas are fixed throughout the NEB calculation. The first replica is the original GB configuration without or with vacancies. The end replica is a configuration in which the entire GB has migrated by a step with the same shear strain as the first replica. We prepare two candidate initial configurations or follow two initialization methods. Method 1 starts with a linear interpolation between the first replica and the end replica. In method 2, the initial intermediate replicas are generated with disconnection loops in the form
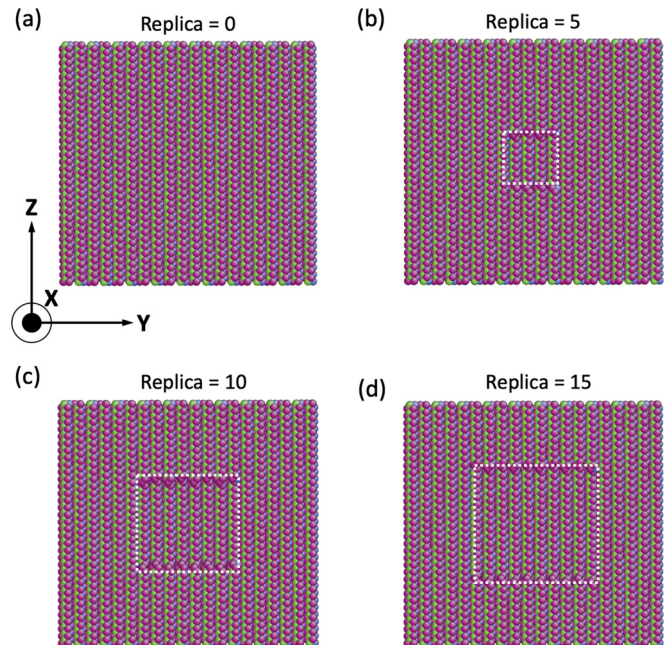

FIG. 2. Top view of several initial replicas for method 2 in our 3D NEB calculations. Disconnection nucleates in the form of similar rectangles (denoted by white dotted line) with respect to the GB shape and expands gradually to the entire GB area. Atoms with CN = 12 are removed, thereby showing the GB in between the top and bottom surfaces.

of similar rectangles, as shown in Fig. 2. To be specific, the disconnection loop of replica i $(1, 2, \ldots, N)$ has size $(\frac{i}{N})^{2/3}L_Y \times (\frac{i}{N})^{2/3}L_Z$, where L_Y and L_Z are the dimensions of the GB in the Y and Z directions, respectively. For each value of shear stress, we choose the converged MEP with a lower energy barrier between these two methods. At low shear stress ($\tau < 450 \, \text{MPa}$), methods 1 and 2 result in different MEPs. Specifically, method 2 yields a lower energy barrier than method 1. At high shear stress ($\tau > 450 \, \text{MPa}$), which is the range we are interested in, both methods yield the same MEP, which verifies the reliability of the NEB calculations.

C. Vacancy formation energy in a GB

The vacancy formation energy in a GB is defined as the energy required to move an atom from a certain GB site α to a perfect lattice site far away from the GB, i.e.,

$$E_f^\alpha = E_{GB}^\alpha - E_{GB} + E_c, \quad (1)$$

where E_{GB}^α is the energy of a defective GB with a monovacancy at site α, E_{GB} is the energy of the initial perfect GB, and E_c is the cohesive energy.

Table I summarizes the vacancy formation energies at select sites [as shown in Fig. 1(b)] in the GB according to

TABLE I. Vacancy formation energies at different GB sites.

Site	1	3	4	5	6	8	9
E_f (eV)	0.172	1.146	1.393	0.849	1.248	1.292	1.248

Eq. (1). It is seen that the vacancy formation energies vary widely from site to site. For most GB sites, the vacancy formation energies are much lower than that in the bulk (i.e., 1.272 eV [39]). However, there are still some GB sites, such as site 8, that have a higher vacancy formation energy than a perfect lattice site. It should be noted that for some sites, such as sites 2 and 7, the GB does not support vacancies at all. In other words, when an atom is removed from either site (2 or 7) to form a vacancy, the atom located in the nearest site 1 would fill the vacancy during the energy minimization process. Thus, the vacancy moves to site 1. The most important observation is that there exists a pair of energy-favorable vacancy formation sites 1 and 1′ with formation energy (i.e., 0.172 eV) which is much lower than any other GB sites. This indicates that for dilute vacancy concentration, most vacancies should be located at sites 1 and 1′ after enough diffusion time.

Following the previous study [40], the concentration c_α of vacancies at a site α in a GB is defined by

$$c_\alpha = \exp\left(-\frac{E_f^\alpha - T S_f^\alpha}{k_B T}\right). \quad (2)$$

Here, E_f^α is the vacancy formation energy at site α, S_f^α is the formation entropy, k_B is the Boltzmann constant, and T is the temperature. In this study, the interaction between vacancies is neglected. Experimentally [41], the factor $\exp(\frac{S_f^\alpha}{k_B})$ ranges between 2 and 10, which is consistent with previous studies [40]. Here, we adopt the upper bound to make the effect of vacancies more prominent. For the 3D simulation cell, as shown in Fig. 1, a total of 680 candidate sites are energetically favorable (i.e., site 1). So according to Table I and Eq. (2), it is estimated that there are, at most, nine energy-favorable vacancies in the GB in thermodynamic equilibrium at room temperature (i.e., 300 K). Accordingly, we start with nine vacancies each located at a neighboring site 1, as shown in Fig. 3. It is worth noting that the vacancies are discrete, individual point defects that remain well separated and embedded in the GB after equilibration.

III. RESULTS

A. Vacancy-enhanced migration

Figure 4 shows the NEB results for GB migration in a 3D simulation cell without and with vacancies. Figure 4(a) shows the converged MEP for shear-coupled migration of a perfect GB (red circles) and the same GB with vacancies (blue squares) at shear stress $\tau = 529$ MPa. In all the MEPs presented here, the reaction coordinate is defined as the normalized path length along the MEP, and the energy of the first replica on the MEP is taken to be zero. It is evident that the vacancies reduce the activation energy from 1.80 eV (red solid circle) to 1.52 eV (blue solid square). Figure 4(b) shows the associated MEPs as a function of the nucleation radius. The atomistic configurations in Figs. 4(c) and 4(d) are the first states, corresponding to a local energy minimum on the MEPs. Figure 4(e) presents the atomistic configuration at the saddle-point state for migration of a perfect GB. It is seen that the shape of the disconnection loop is very close to a circular shape generated by the migration of discrete kite-shaped units. Consistent with prior theoretical prediction
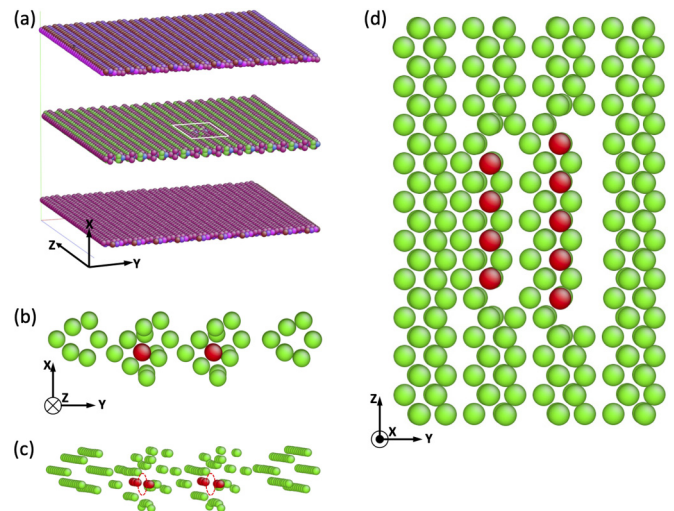

FIG. 3. Simulation setup and corresponding atomic configuration with nine vacancies located in the GB. (a) Simulation cell which is identical to that shown in Fig. 1(a), except with nine vacancies in the GB. Atoms with CN = 12 are removed, thereby showing the GB in between the top and bottom surfaces. (b)–(d) Different views of the atomistic structure of a portion of the GB depicted by the white square in (a). Atoms in the same column as the vacancies are labeled red; atoms in the neighboring columns are labeled green. (b) shows the projection of the GB atoms in the X-Y plane. Vacancy sites are denoted by red circles in (c), in which there are four vacancies in the left column and five in the right, making a total of nine vacancies. (d) shows the discrete vacancy positions in the Y-Z plane.

[4], the disconnection is nucleated in the form of a loop for the 3D case. Figure 4(f) shows the atomistic configuration at the saddle-point state for a GB with vacancies. Since the disconnection loop would intercept as many vacancies as possible (to maximally reduce the line tension and energy barrier, as will be explained later), the disconnection loop would deviate a little but still remain close to a circular shape. The results reveal that the disconnection loop nucleates around the vacancies (denoted by a white circle) and then propagates, eventually resulting in GB migration (see [42]).

The nucleation and growth of the disconnection loop can be quantitatively described by the 3D disconnection model [4,43]. According to the model, the total energy to form a disconnection loop with radius R is given by

$$E(R) = 2\pi R \bar{\Gamma}_s h + E_{loop} - p\pi R^2. \quad (3)$$

The first term is the excess energy arising from the disconnection step, where $\bar{\Gamma}_s$ is the effective line tension and h is the step height, which is 0.255 nm [24] for the $\Sigma 13$ GB. The second term denotes the elastic energy of the disconnection loop, which can be exactly expressed as [44]

$$E_{loop} = 2\pi R \frac{2-\nu}{2(1-\nu)} \frac{\mu b^2}{4\pi} \left[-\ln\left(\tan\frac{\rho}{4R}\right) - 2\cos\frac{\rho}{2R}\right]. \quad (4)$$

Here, the Voigt average Poisson's ratio, $\nu = 0.324$, and the Voigt average shear modulus, $\mu = 55.2$ GPa, are elastic properties of the material. The values are taken for Cu based on the EAM potential used [38]. The Burgers vector b equals 0.1 nm [24], and ρ is the core radius of the disconnection
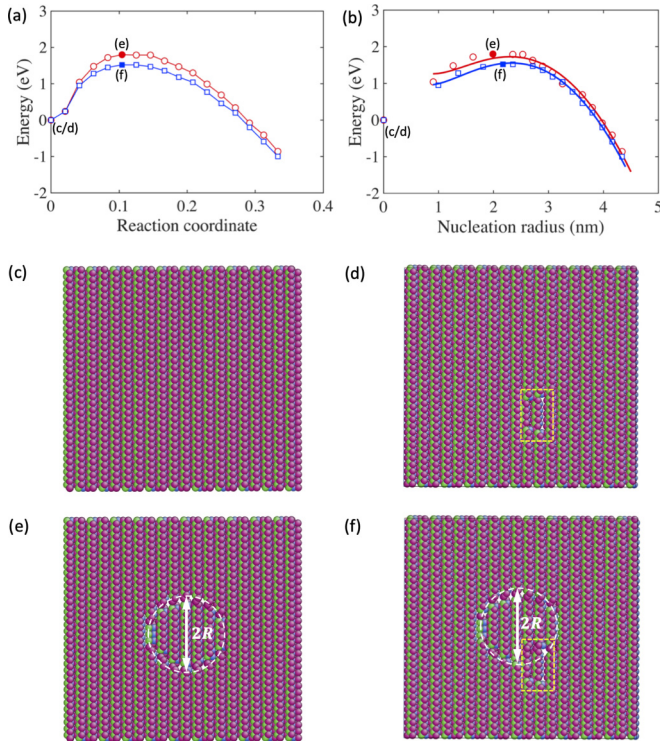
FIG. 4. Three-dimensional NEB results for GB migration without and with nine vacancies under an applied shear stress $\tau = 529$ MPa. (a) MEPs of GB migration without vacancies (red circles) and with nine vacancies (blue squares). (b) Associated MEPs as a function of the nucleation radius. (c) and (d) Top views of atomistic configurations for the first replicas along the MEP for GBs without and with vacancies. (e) and (f) Top views of atomistic configurations for saddle-point states along the MEP for GBs without and with vacancies. Their corresponding energies are plotted as solid red circles and blue squares in (a) and (b). In (e) and (f), the disconnection diameter is denoted by 2R. White dashed circles serve as guides to show circle-shaped nuclei. In (d) and (f), sites with vacancies are denoted by yellow dashed rectangles.

loop. The last term in Eq. (3) is the work done by the driving stress p, which equals $\tau \beta$, where τ is the applied shear stress. Figure 4(b) plots the associated disconnection loop energy $E(R)$ as a function of the disconnection loop radius R without and with vacancies. The discrete points are simulation results, whereas the solid lines are based on Eqs. (3) and (4) with $\bar{\Gamma}_s$ and ρ used as fitting parameters. It is worth emphasizing that the excellent agreement between our atomistic simulations and the theoretical results provides direct verification of the 3D disconnection model for GB migration. Furthermore, it is interesting to note that the model maintains its validity even in the presence of vacancies, suggesting that the disconnection mechanism for GB migration remains the same. The disconnection core radius ρ is estimated to be 1.5 ± 0.1 nm in both cases (i.e., without and with vacancies), which is consistent with a prior work [45]. This implies that the 3D disconnection model, being a continuum model, is likely to break down when the nucleation radius is smaller than the disconnection core radius, which is about 1.5 nm for our case. Indeed, as seen in Fig. 4(b), the curve for the disconnection model
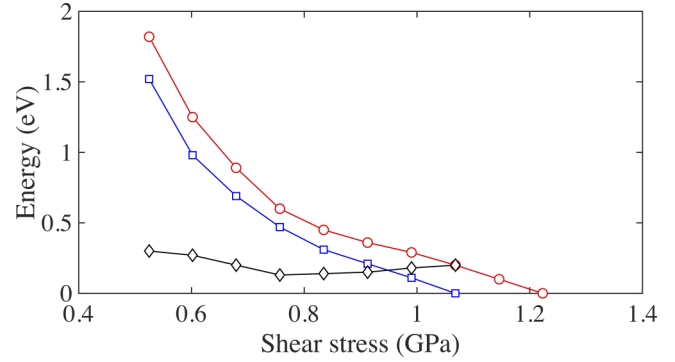

FIG. 5. Three-dimensional NEB calculations for the energy barrier of GB migration without (red circles) and with vacancies (blue squares) as a function of stress and the energy reduction due to vacancies (black diamonds).

starts deviating from the simulation results around 1 nm. $\bar{\Gamma}_s$ decreases from 345 mJ/m^2 for a perfect GB to 314 mJ/m^2 in the presence of vacancies. This suggests that the vacancies weaken the disconnection line tension, thereby reducing the energy barrier for GB migration. It is also consistent with the observation that the disconnection loop nucleates around vacancies [see Fig. 4(f)]. Figure 5 reports the stress-dependent energy barrier for GB migration without and with vacancies using NEB calculations. The reduction in the energy barrier due to vacancies is in the range of 0.13–0.30 eV.

B. Effects of vacancy distribution and number

In order to verify the vacancy-enhanced migration, we have studied three different cases of vacancy distributions (different arrangements of nine vacancies). Figure 6 shows the stress-dependent activation energies for the GB without vacancies and with various vacancy configurations. The reduction in the energy barrier due to vacancies is evident for all three vacancy distributions. Here, vacancy distribution 1 refers to the atomistic configuration shown in Fig. 3. The atomistic configurations of vacancy distributions 2 and 3 are shown in Figs. 7 and 8, respectively. Specifically, distribution 2 consists of nine vacancies arranged in a single row and occupying site
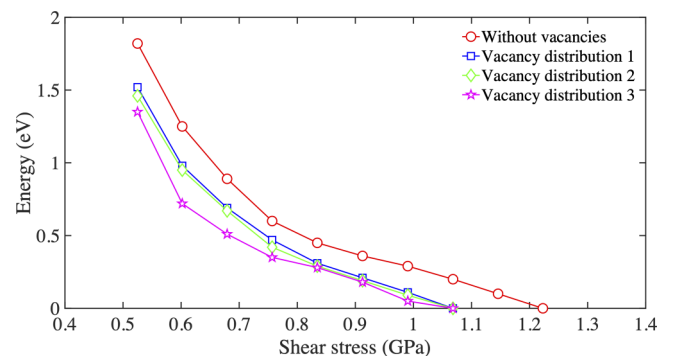

FIG. 6. Three-dimensional NEB calculations for the energy barrier of GB migration without vacancies (red circles) and with vacancy distribution 1 (blue squares), distribution 2 (green diamonds), and distribution 3 (pink pentagrams) as a function of stress.
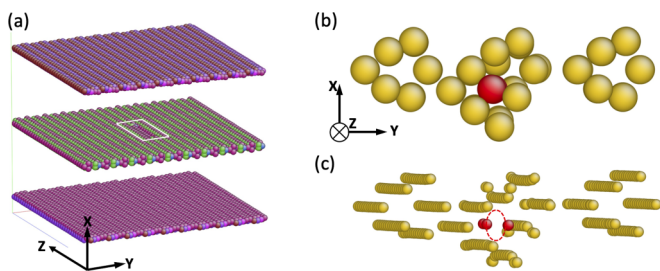
FIG. 7. Simulation setup and corresponding atomic configuration of nine vacancies with distribution 2. (a) Simulation cell which is identical to those shown in Fig. 1(a), except with nine vacancies in the GB. Atoms with CN = 12 are removed, thereby showing the GB in between the top and bottom surfaces. (b) and (c) Inset images of the atomistic structure of a portion of the GB depicted by the white square in (a). Here, atoms in the same column as vacancies are labeled red; other column atoms are labeled yellow. Vacancy sites are denoted by red circles in (c), in which all the vacancies are in the same column.

1, whereas distribution 3 consists of nine vacancies arranged randomly. It is worth noting that the vacancies are discrete and do not collapse into a void even for distribution 2.

In order to study the effect of the number of vacancies, we use the random distribution of vacancies and vary the number from 1 to 11. Figure 9 shows the activation energies without
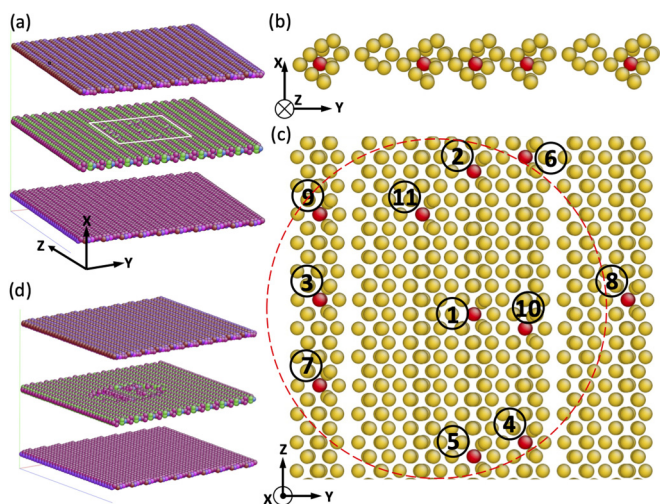

FIG. 8. Simulation setup and corresponding atomic configuration of randomly arranged vacancies with distribution 3. (a) Simulation cell which is identical to that shown in Fig. 1(a), except with nine vacancies [numbered 1 to 9 in (c)] in the GB. Atoms with CN = 12 are removed, thereby showing the GB in between the top and bottom surfaces. (b) and (c) Atomistic structure of a portion of the GB [depicted by a white square in (a)] showing the arrangement of 11 vacancies. Here, atoms in the same direction as the vacancies projected in the X-Y plane are labeled red; other atoms are labeled yellow. Vacancy positions in the Y-Z plane are labeled by numbers from 1 to 11. (d) Atomistic configuration of the saddle-point state along the MEP of the GB with the first nine vacancies [numbered 1 to 9 in (c)] under an applied shear stress $\tau = 529$ MPa. The red dashed circle in (c) schematically shows the disconnection loop connecting as many vacancies as possible at the configuration shown in (d).
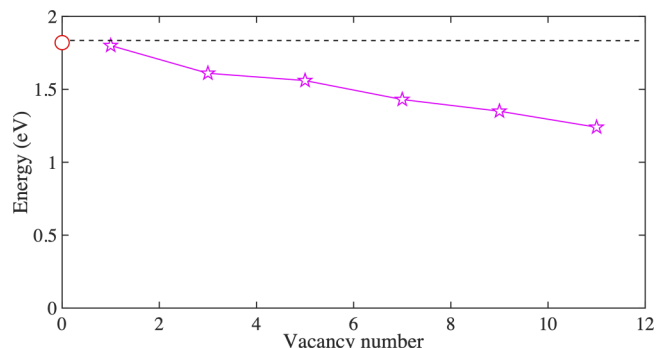

FIG. 9. Three-dimensional NEB calculations for the energy barrier of the GB migration without vacancies and with a varying number of vacancies under an applied shear stress $\tau = 529$ MPa. The black dashed line is provided as a guide to the eyes and corresponds to the energy barrier without vacancies.

vacancies and with different numbers of vacancies arranged randomly. Here, number i means that there are i vacancies located at sites 1 from positions 1 to i, as shown in Fig. 8(c). It is evident that the energy barrier decreases with increasing vacancies. The reduction of the energy barrier depends on how many vacancies participate in the nucleation process in the saddle-point state, or, in other words, how many vacancies are located near the disconnection loop and interact with it. Here, the activation volume is the disk-shaped volume with radius R and height h or the projected area of the GB with radius R. Quantitatively, it is defined as the derivative of the energy with respect to the applied stress [46] and usually decreases with increasing stress. In Fig. 8(d), besides the number 1 vacancy, the other eight vacancies $(2, 3, \ldots, 9)$ have the opportunity to be simultaneously located around the disconnection loop at the saddle-point state [as schematically shown by the red dashed circle in Fig. 8(c)]. It follows that they can reduce the line tension of the disconnection and the energy barrier of GB migration as much as possible so that the energy reduction is largest among all three cases in Fig. 6 under an applied shear stress of $\tau = 529$ MPa. With increasing stress, the activation volume eventually becomes so small that only a few vacancies (one or two for any vacancy distribution) need to be located around the dislocation loop to reduce the energy barrier. This explains why, at high stress, the reductions in the energy barrier for different vacancy distributions are very close to each other. However, a more quantitative study of the dependence of the activation barrier on the vacancy distribution entails further theoretical analysis and simulations which will be part of our future work.

IV. DISCUSSION

A. Atomistic mechanism for vacancy-enhanced migration

In order to elucidate the elementary mechanism of vacancy-enhanced migration, we employ quasi-2D simulations, where the out-of-plane thickness of the simulation cell is very small and has periodic boundary conditions (see Fig. 10). We recall that site 1 is the most energetically favorable for vacancy formation. Using energy minimization, Fig. 11 shows the relaxed configuration of the GB atoms after
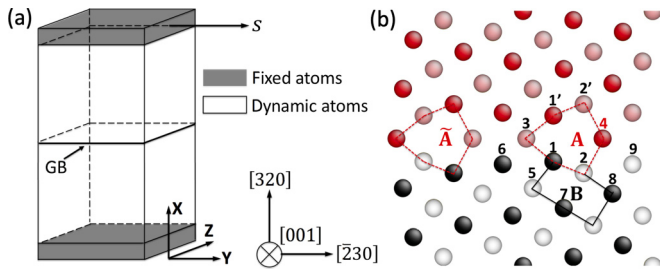
FIG. 10. (a) Schematic of the 2D simulation cell. The size of the 2D simulation cell is $103 \times 13 \times 14 \, \text{Å}^3$. (b) Atomistic configuration of the $\Sigma 13(320)$ GB projected in the (X, Y) plane: Black (gray) and red (pink) atoms belong to different grains. Black (red) and gray (pink) atoms are in two alternate (100) planes. Candidate vacancy sites are denoted by the numbers from 1 to 9.

one atom is removed from site 1. Several nearest-neighbor atoms surrounding the vacancy, including atoms at site 2 and site $1'$, relax significantly towards the vacancy, which is consistent with previous studies [40,47]. It is this displacement towards the vacancy site that triggers GB migration via transformation of the structural units from A to B under shear deformation.

Figure 12 shows the NEB simulations of a 2D bicrystal with a monovacancy located at site 1. Converged MEPs for GB migration without and with vacancies in Fig. 12(a) are denoted by red and blue circles, respectively, at the same shear displacement ($s = 0.066 \, \text{nm}$). The MEP for the GB without vacancies matches that reported by [24], which verifies our NEB calculation results. In the presence of a monovacancy, the activation energy for GB migration decreases by almost 50% from 0.29 to 0.16 eV. For intermediate configurations along the MEP for the perfect GB, we refer the reader to [24]. Figures 12(b)–12(g) show intermediate GB structures along the MEP for migration of a GB with a monovacancy. The GB structure in Fig. 12(b) is the first replica, corresponding to a local energy minimum on the MEP. The kite-shaped unit A is represented by red lines, while the black lines denote the regular structural unit B. The green lines denote the bond
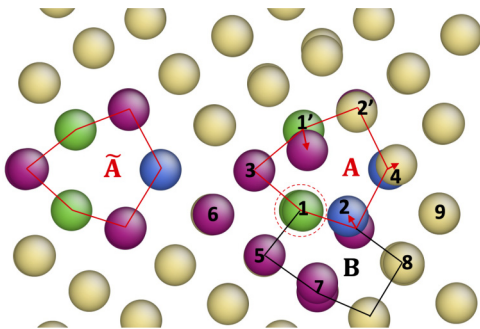

FIG. 11. Relaxed structure of the $\Sigma 13(320)$ GB with a monovacancy at site 1. Atoms are colored according to the coordination number. The red dotted circle marks the vacant site. Since there is a total of four atoms for each site in the Z direction, the introduction of one vacancy still leaves three atoms, leading to visible atoms projected in the (X, Y) plane (green atoms marked as site 1). Relaxation of atoms surrounding the vacant site is denoted by red arrows.
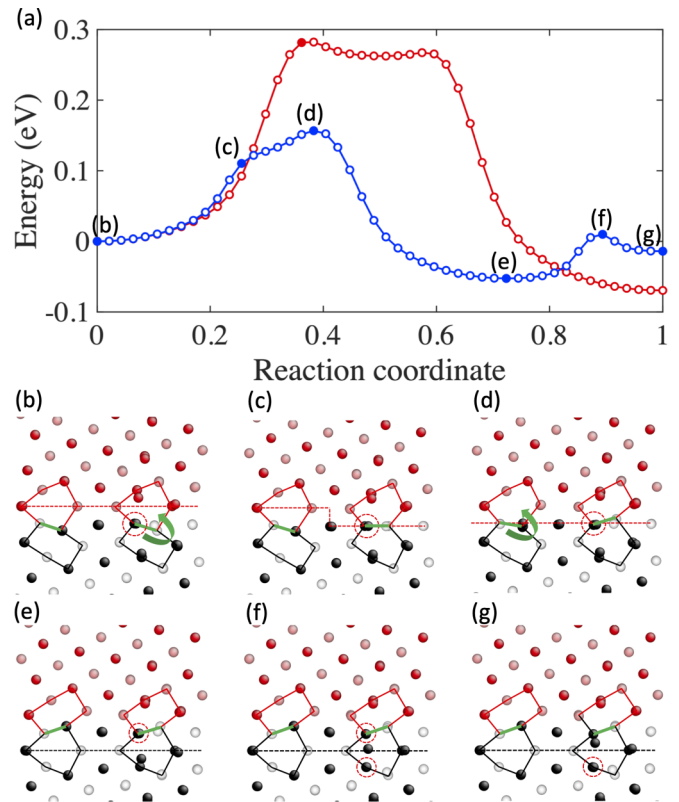

FIG. 12. Two-dimensional NEB results for the GB migration without and with monovacancy at a shear displacement $s = 0.066 \, \text{nm}$. (a) MEPs of GB migration without a vacancy (red open circles) and with a vacancy (blue open circles). (b)–(g) Projection in the (x, y) plane of atomic configurations of replicas along the MEP for the GB with a vacancy. Their corresponding energies are plotted as solid blue circles in (a). Red and black dotted lines are guides to the eyes through labeling the transient GB positions. For atomic configurations along the MEP for a perfect GB without vacancy, we refer the reader to [24].

between two atoms that belong to the two structural units. The monovacancy is marked by a red dashed circle at site 1 of unit A.

First, the relaxation of atoms (at sites 2 and $1'$) around the vacancy, in addition to the applied shear stress, triggers an anticlockwise rotation of the green bond depicted by the green arrow [Fig. 12(b)]. This initiates a transformation of the lattice structural unit B into a kite-shaped GB unit A [Fig. 12(c)]. A concomitant step in the GB (depicted by the red dotted line) is observed between the left and right kite-shaped structural units. At the saddle-point state [Fig. 12(d)], the green bond continues to rotate and completes the transformation between structural units A and B. This vacancy-enhanced A-B unit transformation on the right facilitates the unit transformation on the left, thus yielding a lower energy barrier of 0.16 eV. When the transformation of the left structural units A-B is completed [Fig. 12(e)], it results in a local minimum energy state along the MEP [Fig. 12(a)]. After this GB migration, the monovacancy diffuses to site 1 of the new GB [Figs. 12(e) and 12(g)]. The associated energy barrier for vacancy diffusion is the relative energy difference between the states (e) and (f) along the MEP [Fig. 12(e)], yielding 0.08 eV. It is worth
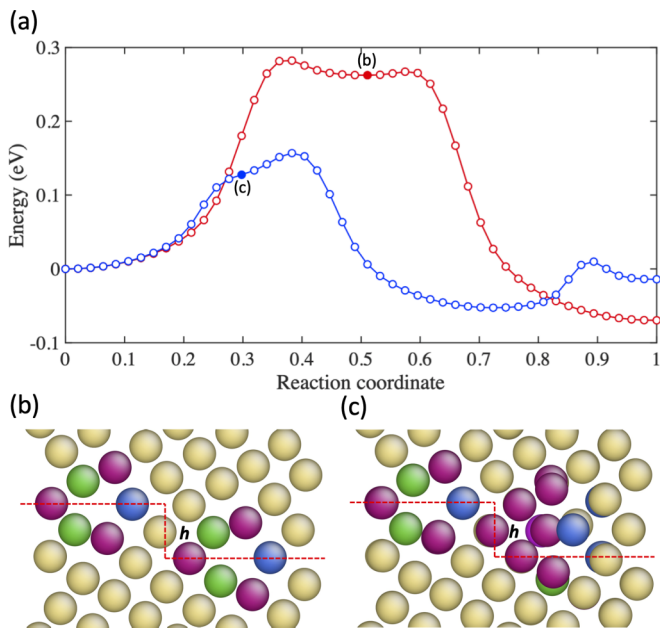
FIG. 13. Two-dimensional NEB results for the GB migration without and with monovacancy at a shear displacement $s = 0.066$ nm. (a) MEPs of GB migration without a vacancy (red open circles) and with a vacancy (blue open circles). (b) and (c) Atomistic configurations associated with the formation of step h without and with a vacancy. Atoms are colored according to the coordination number. Red dotted lines are guides to the eyes through labeling step h.

noting that the energy barrier of the vacancy diffusion in the lattice is around 0.7 eV [48]. As such, this monovacancy prefers to move with the GB and continues to facilitate subsequent GB migration.

B. Line tension and varying GBs

The "effective line tension" in this work is the average energy penalty associated with a disconnection step h. From an atomistic view, the vacancies serve as energetically favorable sites for disconnection nucleation in a grain boundary, thereby facilitating shear-coupled migration. From a mesoscopic and defect-level perspective, as shown in Figs. 13(b) and 13(c), it is the vacancy that reduces the interaction between a "perfect" kite-shaped unit and an adjacent "defective" kite-shaped unit, leading to a lower energy penalty for the same disconnection step h. As such, it is reasonable to attribute the reduction of the energy barrier to the reduction of the line tension at the mesoscopic level, as shown in Eq. (3).

To study the effect of vacancies on different GBs, we also examined several other CSL high-angle GBs (as shown in Fig. 14) using quasi-2D NEB calculations. It is seen from Fig. 15 that vacancies lower the activation barrier for migration in all cases. It also reveals that the reduction of the line tension and energy barrier is associated with the spacing between adjacent kite-shaped structural units forming each GB.

C. MD simulations at finite temperature

We performed several MD simulations to verify the vacancy-enhanced migration at finite temperature, both in two
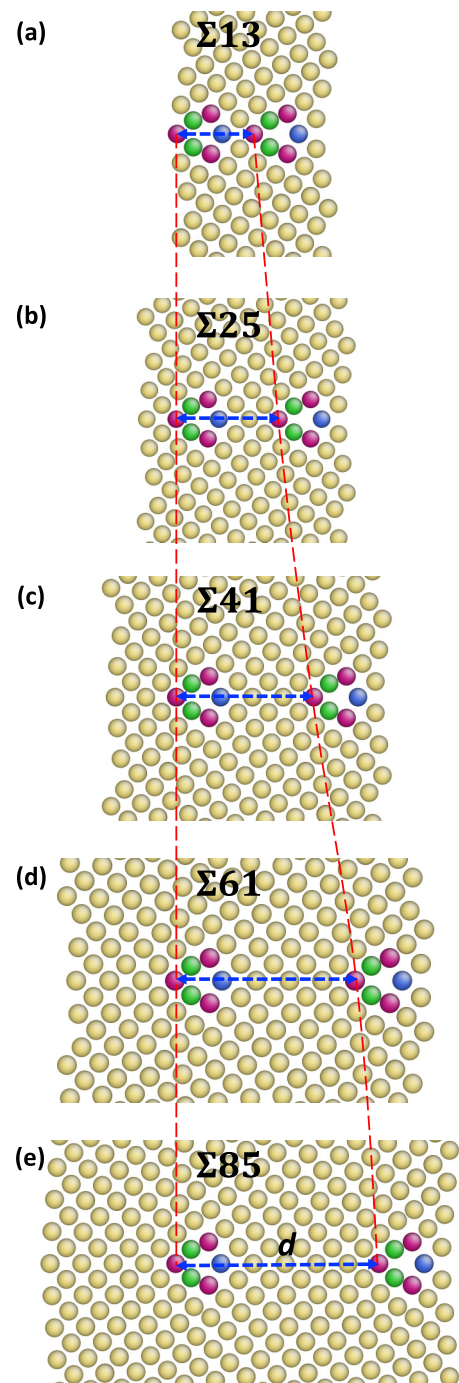

FIG. 14. Atomistic configurations of the simulation cells with (a) Σ13(320), (b) Σ25(430), (c) Σ41(540), (d) Σ61(650), and (e) Σ85(760) GBs. Atoms are colored according to the coordination number (green: CN = 10; purple: CN = 11; yellow: CN = 12; blue: CN = 13). For each GB, the spacing between two adjacent kite-shaped structure units is defined by d. The two dashed red lines serve as guides to show how the spacing d changes with the GB structure.

dimensions (Fig. 10) and three dimensions (Fig. 3) under constant shear stress. To implement constant stress conditions, we follow the method used for MD simulation of dislocation mobility in [49]. Multiple simulations (20 independent samples) were performed in order to calculate the ensemble
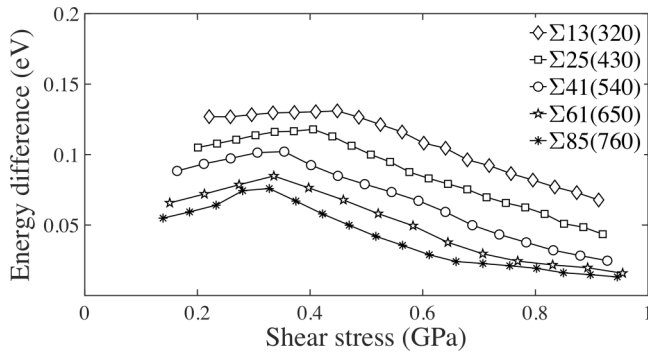
FIG. 15. Energy difference (i.e., the reduction of energy barrier) in the presence of the monovacancy versus applied shear stress for various GBs shown in Fig. 14.

mean values. In order to accurately extract the average GB displacement for each time interval, we dynamically capture the GB profile based on the coordination number of each atom. A similar method was utilized in other works [7,8,10]. Figure 16 shows the shear-coupled GB migration at room temperature in 2D and 3D simulation cells without and with a monovacancy. For the 2D simulation cell, it is observed that GB migration in the presence of a monovacancy is almost one order faster than that GB without a vacancy under shear stress $\tau = 116$ MPa. Vacancy-enhanced migration is also observed for a 3D simulation cell with nine vacancies under shear stress $\tau = 316$ MPa. Thus, these MD simulations clearly demonstrate the following: (1) The discrete vacancies do not diffuse away from the GB but instead stay in the GB as the boundary migrates. Thus, the effect of vacancies on the boundary migration continues. (2) The presence of vacancies facilitates shear-coupled GB migration.

V. CONCLUDING REMARKS

NEB calculations provide excellent verification of the 3D disconnection model and furnish quantitative evidence that vacancies facilitate shear-coupled migration of a certain class of GBs. Consistent with prior theoretical prediction [4], 3D atomistic modeling reveals that GB migration occurs via nucleation and growth of a disconnection in the form of a dislocation loop on the GB. Thus, from a continuum mechanics viewpoint, vacancies tend to weaken the line tension of a disconnection loop, thereby promoting shear-coupled migration. Three-dimensional as well as quasi-2D simulations reveal that, from an atomistic viewpoint, vacancies serve as energetically favorable sites for disconnection nucleation of the GB, thereby facilitating shear-coupled migration.

This study opens avenues for investigating the role of vacancies in migration and mobility of other GB structures.
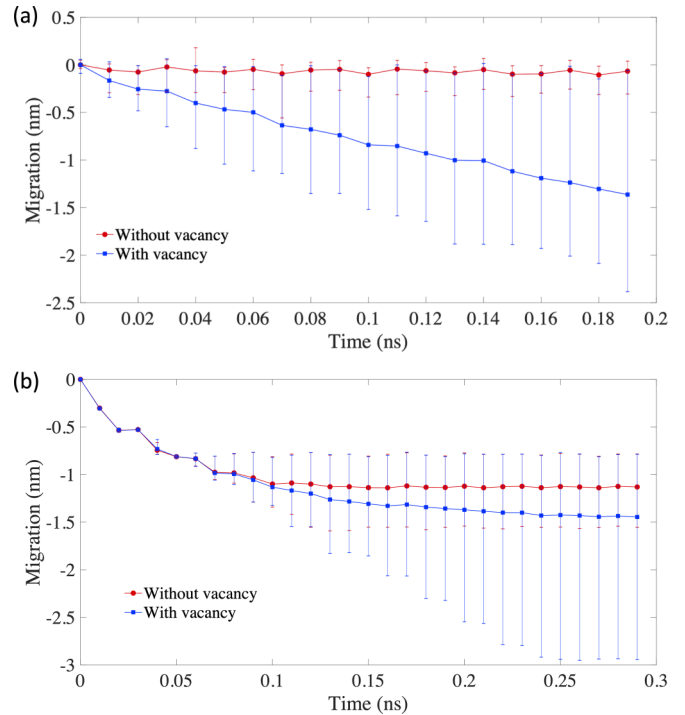

FIG. 16. MD simulations of shear-coupled GB migration at room temperature (a) under constant shear stress $\tau = 116$ MPa for a 2D simulation cell and (b) under constant shear stress $\tau = 316$ MPa for a 3D simulation cell. Error bars for each time interval show the fluctuation of GB displacement of 20 independent samples. Solid lines (blue and red) show the mean values.

Moreover, the 3D NEB method employed here can be used to gain insights into the role of other types of defects on GB migration and, consequently, properties of polycrystalline materials. We believe that if the kite-shaped unit of the grain boundary retains its stable structure on adding dilute vacancies, we should see vacancy-enhanced migration. However, it is possible that there may be a change in deformation mechanism for GB migration when we look at GBs beyond this class. More systematic simulations would be needed for this study, which is beyond the scope of this paper and will be pursued in our future work.

[1] A. P. Sutton and R. W. Balluffi, *Interfaces in Crystalline Materials* (Oxford University Press, Oxford, 2007).

[2] G. Gottstein and L. S. Shvindlerman, *Grain Boundary Migration in Metals: Thermodynamics, Kinetics, Applications* (CRC Press, Boca Raton, FL, 1999).

[3] H. Riedel, *Fracture at High Temperatures* (Springer, Berlin, 1987).

[4] J. Han, S. Thomas, and D. Srolovitz, Prog. Mater. Sci. **98**, 386 (2018).

[5] A. T. Lim, M. Haataja, W. Cai, and D. J. Srolovitz, Acta Mater. **60**, 1395 (2012).

[6] V. Agrawal and K. Dayal, J. Mech. Phys. Solids **85**, 291 (2015).

[7] D. Chen and Y. Kulkarni, MRS Commun. **3**, 241 (2013).

[8] Z. T. Trautt, M. Upmanyu, and A. Karma, Science **314**, 632 (2006).

[9] S. M. Foiles and J. J. Hoyt, Acta Mater. **54**, 3351 (2006).

[10] C. Deng and C. A. Schuh, Phys. Rev. Lett. **106**, 045503 (2011).

[11] D. Chen and Y. Kulkarni, Phys. Rev. Mater. **2**, 093605 (2018).

[12] S. Huang, D. Chen, D. L. McDowell, and T. Zhu, npj Comput. Mater. **3**, 28 (2017).

[13] Z. Wang, Q. Li, Y. Li, L. Huang, L. Lei, M. Dao, J. Li, S. Suresh, and Z. Shan, Nat. Commun. **8**, 1108 (2017).

[14] Y. Wei, Y. Li, L. Zhu, Y. Liu, X. Lei, G. Wang, Y. Wu, Z. Mi, J. Liu, H. Wang, and H. Gao, Nat. Commun. **5**, 3580 (2014).

[15] X. W. Gu, Z. Wu, Y. W. Zhang, D. J. Srolovitz, and J. R. Greer, Nano Lett. **13**, 5703 (2013).

[16] A. Dasgupta, P. Sharma, and K. Upadhyayula, Int. J. Damage Mech. **10**, 101 (2001).

[17] N. Admal, G. Po, and J. Marian, Int. J. Plast. **106**, 1 (2018).

[18] I. Beyerlein, M. Demkowicz, A. Misra, and B. Uberuaga, Prog. Mater. Sci. **74**, 125 (2015).

[19] S. Thomas, K. Chen, J. Han, P. Purohit, and D. Srolovitz, Nat. Commun. **8**, 1764 (2017).

[20] J. Cahn and J. Taylor, Acta Mater. **52**, 4887 (2004).

[21] J. Cahn, Y. Mishin, and A. Suzuki, Acta Mater. **54**, 4953 (2006).

[22] E. R. Homer, S. M. Foiles, E. A. Holm, and D. L. Olmsted, Acta Mater. **61**, 1048 (2013).

[23] F. Mompiou, D. Caillard, and M. Legros, Acta Mater. **57**, 2198 (2009).

[24] A. Rajabzadeh, F. Mompiou, M. Legros, and N. Combe, Phys. Rev. Lett. **110**, 265507 (2013).

[25] N. Combe, F. Mompiou, and M. Legros, Phys. Rev. B **93**, 024109 (2016).

[26] N. Combe, F. Mompiou, and M. Legros, Phys. Rev. Mater. **1**, 033605 (2017).

[27] N. Combe, F. Mompiou, and M. Legros, Phys. Rev. Mater. **3**, 060601 (2019).

[28] Q. Zhu, G. Cao, J. Wang, C. Deng, J. Li, Z. Zhang, and S. X. Mao, Nat. Commun. **10**, 156 (2019).

[29] G. Henkelman, B. R. Uberuaga, and H. Jonsson, J. Chem. Phys. **113**, 9901 (2000).

[30] T. Zhu, J. Li, A. Samanta, H. G. Kim, and S. Suresh, Proc. Natl. Acad. Sci. U.S.A. **104**, 3031 (2007).

[31] J. P. Hirth and R. C. Pond, Acta Mater. **44**, 4749 (1996).

[32] M. I. Mendelev and D. J. Srolovitz, Model. Simul. Mater. Sci. Eng. **10**, R79 (2002).

[33] N. Du, Y. Qi, P. E. Krajewski, and A. F. Bower, Acta Mater. **58**, 4245 (2010).

[34] H. Sun and C. Deng, Comput. Mater. Sci. **93**, 137 (2014).

[35] D. Chen, T. Ghoneim, and Y. Kulkarni, Appl. Phys. Lett. **111**, 161606 (2017).

[36] D. Song, X. Li, J. Xue, D. Hui, and Z. Jin, Philos. Mag. Lett. **94**, 361 (2014).

[37] S. J. Plimpton, J. Comput. Phys. **117**, 1 (1995).

[38] Y. Mishin, M. J. Mehl, D. A. Papaconstantopoulos, A. F. Voter, and J. D. Kress, Phys. Rev. B **63**, 224106 (2001).

[39] A. Suzuki and Y. Mishin, Interface Sci. **11**, 425 (2003).

[40] M. R. Sørensen, Y. Mishin, and A. F. Voter, Phys. Rev. B **62**, 3658 (2000).

[41] W. Cai and W. Nix, *Imperfections in Crystalline Solids* (Cambridge University Press, Cambridge, 2016).

[42] See Supplemental Material at http://link.aps.org/supplemental/10.1103/PhysRevMaterials.4.033602 for videos of GB migration with and without vacancies.

[43] C. P. Race, J. von Pezold, and J. Neugebauer, Phys. Rev. B **89**, 214110 (2014).

[44] J. P. Hirth and J. Lothe, *Theory of Dislocations* (Krieger Publishing, Malabar, Florida, 1992).

[45] S. Xu, L. Xiong, Y. Chen, and D. McDowell, J. Mech. Phys. Solids **96**, 460 (2016).

[46] T. Zhu and J. Li, Prog. Mater. Sci. **55**, 710 (2010).

[47] G. Lu and N. Kioussis, Phys. Rev. B **64**, 024101 (2001).

[48] T. Zhu, J. Li, and S. Yip, in *Nano and Cell Mechanics*, Wiley Online Library (Wiley, Hoboken, NJ, 2013), pp. 313–338.

[49] D. L. Olmsted, L. G. Hector, Jr., W. A. Curtin, and R. J. Clifton, Model. Simul. Mater. Sci. Eng. **13**, 371 (2005).